Fabrication and Photoluminescence Studies of Tin Vacancy Centers in CVD Diamond

Rani Mary Joy,[1,2,*] Miquel F. Cherta,[3,4] Omar J. Y. Harb,[3,4] Hendrik Jeuris,[1,2] Rozita Rouzbahani,[1,2] Jan D'Haen,[1,2] Stéphane Clemmen,[3,4,5,6] Dries Van Thourhout,[3,4] Danny E. P. Vanpoucke,[1,2] Paulius Pobedinskas,[1,2] and Ken Haenen[1,2]

[1] *Institute for Materials Research (IMO), Hasselt University, Wetenschapspark 1, 3590 Diepenbeek, Belgium*
[2] *IMOMEC, IMEC vzw, Wetenschapspark 1, 3590 Diepenbeek, Belgium*
[3] *Photonics Research Group, INTEC-department, Ghent University-IMEC, 9052 Ghent, Belgium*
[4] *Center for Nano- and Biophotonics (NB-Photonics), Ghent University, 9052 Ghent, Belgium*
[5] *OPERA-Photonique CP 194/5, Université Libre de Bruxelles (ULB), 1050 Brussels, Belgium*
[6] *Laboratoire d'Information Quantique CP 224, Université Libre de Bruxelles (ULB), 1050 Brussels, Belgium*

Group IV color centers in diamond are promising single-photon sources for quantum information processing and networking. The tin vacancy (SnV) center is especially notable for its long spin coherence times at cryogenic temperature above 1 K. While SnV centers have been created using various methods, their in situ growth using microwave plasma-enhanced chemical vapor deposition (MW PE CVD) remains underexplored. In this study, SnV centers, identified by a zero-phonon line 620 nm, were synthesized in nanocrystalline and free-standing microcrystalline diamond at substrate temperatures of 850 °C and 750 °C, using tin oxide (SnO_2) as the dopant source. We investigate the effect of substrate temperature on SnV formation in CVD diamond and from photoluminescence results find that lower substrate temperatures enhance both SnV zero-phonon line intensity and spatial uniformity. These findings offer valuable insight into optimizing SnV center fabrication in diamond via the MW PE CVD technique for quantum technology applications.

Advancements in photonic architectures have highlighted the suitability of diamond as a material platform for quantum information processing applications [1–3]. These all-optically controlled diamond systems are primarily based on the nitrogen-vacancy (NV) center due to its extended spin coherence times at room temperature [4]. However, enhancing its optical performance with nano-structures and stability remains a challenge, given the sensitivity of the shallow NV center to the diamond surface [5, 6]. Promising alternatives are the Group IV color centers in diamond that consist of a split vacancy configuration in the diamond lattice with an interstitial Group IV atom. Because of their molecular structure, these color centers exhibit inversion symmetry and, are less affected by first-order electric fluctuations with minimal spectral diffusion making them potential quantum network nodes in an integrated photonics platform [7, 8]. The most widely reported Group IV color centers are the silicon-vacancy (SiV) and germanium-vacancy (GeV) centers in diamond [9]. Compared to SiV and GeV, the tin-vacancy (SnV) center in diamond, with a zero phonon line (ZPL) at ≈ 620 nm, has a long spin coherence time already at temperatures below 2 K [10].

The state-of-the-art fabrication strategies reported for the SnV center in diamond are the high-pressure high-temperature (HPHT), the conventional two-step ion implantation-annealing, and shallow ion implantation-chemical vapor deposition (CVD) overgrowth processes [11–14]. Recently, detonation process have also reported SnV formation in diamond [15]. However, these techniques have multiple steps or result in a combination of micro- and nano-crystals of diamond, which require further processing. On the contrary, the microwave plasma-enhanced chemical vapor deposition (MW PE CVD) technique in the presence of a Sn precursor facilitates a scalable in-situ creation of SnV centers in diamond in a single process step. Thus far, only a few studies report the fabrication of SnV centers in diamond using the MW PE CVD technique. Westerhausen et al. and Sedov et al. have reported the fabrication of SnV centers in diamond using the MW PE CVD technique [16, 17]. Although these reports confirm SnV formation in diamond, the effect of CVD process conditions on the PL properties are currently lacking and forms the primary motivation of this study.

Here, we report the SnV formation in CVD diamond fabricated at different substrate temperatures and mitigate solid dopant related process limitations using a modified substrate holder. Photoluminescence (PL) characteristics of SnV centers in nanocrystalline diamond (NCD) and in free-standing (110)-oriented microcrystalline diamond (MCD) fabricated using the MW PE CVD technique with tin oxide (SnO_2) as the solid dopant source are presented. Our results confirm the formation of SnV centers in diamond, as evidenced by the ZPL observed at ≈ 620 nm. PL analysis shows spatial non-uniformity of SnV formation in all the samples. In addition, a range of PL peaks are observed that could be attributed to the fabrication-induced strain. This correlation is further supported by theoretical studies under hydrostatic conditions, thereby providing a better understanding of the PL spectra observed in this study.

Two types of substrates were used - commercially available (100)-oriented silicon (Si) of dimensions 5 mm × 5 mm × 0.5 mm and free-standing 1 mm thick MCD discs 3 mm in diameter with a mean roughness of

* Corresponding author: rani.maryjoy@uhasselt.be

less than 20 nm. Prior to diamond growth, the Si substrates were cleaned by an exposure to oxygen plasma followed by a detonation nanodiamond seeding step, deionised water rinse and spin-drying steps [18]. The MCD substrates were wet-chemically cleaned in an acetone ultrasonication bath for 10 minutes, followed by boiling in a mixture of sulfuric acid and potassium nitrate (1:1 ratio) for a duration of 1 hour, with subsequent deionized water rinse and nitrogen drying steps.

Diamond growth was carried out on Si substrates in the ASTeX 6500 MW PE CVD system using a process gas mixture of 1 % methane in hydrogen, total gas flow of 500 sccm, working pressure and MW power of 25 Torr and 2000 W, respectively. The substrate and pellet of SnO_2 are placed with a lateral separation of 5 mm (schematic shown in Fig. 1 (a)) and are simultaneously exposed to the diamond growth conditions for a duration of 1 h.

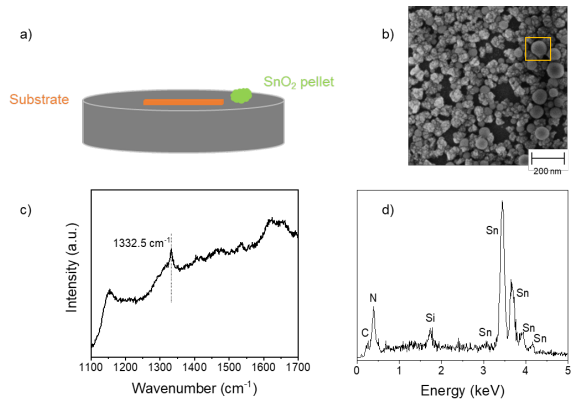


Figure 1. a) Schematic of NCD growth on Si substrate in the presence of SnO_2 pellets, b) SEM shows grains along with spherical features (indicated in yellow), c) Raman spectrum of NCD on Si substrate, and d) EDX analysis on the indicated area of the SEM image shows Sn deposits on the sample surface.

Figures 1(b) and 1(c) show representative scanning electron microscopy (SEM) and Raman spectrum of the sample. Randomly oriented grains along with spherical features are observed in SEM, while the characteristic peak at 1332.5 cm^{-1} confirms diamond formation in the mentioned CVD conditions. Energy dispersive X-ray (EDX) analysis of these spherical features confirms their composition is primarily of Sn (Fig. 1 (d)) and indicates a significant process challenge when using tin oxide as the dopant source. A study has shown that exposure to a hydrogen-rich CVD diamond plasma leads to the reduction of SnO_2 to Sn [19]. With a low melting point of $\approx 231\,^{\circ}C$ [17], Sn deposits on the substrate, thereby partially inhibiting diamond growth, hence a continuous diamond film is not observed in this sample. In addition, temperature measurements on some substrate areas are challenging. Nevertheless, we estimate a growth temperature of $(650 \pm 20)\,^{\circ}C$, measured using a dual wavelength Williamson Pro92 pyrometer. Through trial and error, a lateral separation of 5 mm between the dopant source and the substrate was identified sufficient for diamond growth using the chosen conditions. Smaller separations between the substrate and dopant source led to even lesser areas of diamond growth on the sample surface and was hence not further investigated in this study.

Room temperature PL analysis of the sample confirms SnV formation in diamond, as evidenced by the 620 nm PL peaks observed in Figure 2(a). Moreover, peaks at 613 nm and 631 nm are also observed at room temperature, which motivated a sample PL characterization at a cryogenic temperature of 7.5 K. Figure 2(b) shows examples of the different PL spectra and and figure 2(c) the corresponding histogram of the center wavelength distribution observed in this sample, obtained from a mapping area of 40 µm × 40 µm. From the histogram, it can be seen that the most frequent peak is around 624 nm. The vast majority of the peaks at 624 nm observed in this sample are localized in a region of around 50 μm^2, clearly indicating spatial non-uniformity of SnV formation in the sample (Fig. 2(c) inset shows the PL map). A peak shift of 4 nm, relative to the unstrained SnV ZPL reported in the literature [11], along with broad and uniform linewidth of approximately 0.6 nm is observed for the 624 nm spectral line (purple spectrum of Fig. 2(b)). Our previous study of the GeV center in NCD film has indicated PL peak shifts to be strain-induced [20], while ZPL broadening and masking of the fine structure of SiV centers in diamond have been associated with the dislocations within the diamond lattice [21]. Based on the above, we attribute the ZPL shift and broadening manifested in the 624 nm spectral line as the effect of strain and the polycrystalline morphology of the NCD sample (as evident from the SEM image) on the optical properties of the SnV center.

Although less frequently obeseved relative to the 624 nm PL peak, narrow spectral lines are also detected in this sample (blue and orange spectra of Fig. 2 (b)). These features are similar to the reports of reported Sedov et al [17], indicative of single centers or clusters of few ensembles and will be the focus of future studies.

Interestingly, spectral features with varying full-width at half-maximum (FWHM) are also seen (Fig. 2 (d)). For example, the 622 nm line ranges from below 0.1 nm to above 2 nm. Unlike the 624 nm PL peak, the FWHM variation of the the 622 nm line is not limited to a localized area on the sample but from different locations. Stress=related diamond Raman peak shifts and associated SiVm GeV and SnV centers in diamond have been reported in the literature [17, 20, 22]. To further investigate stress, Raman spectroscopy was performed on the sample, but significant shifts in diamond Raman peak are not observed. Nevertheless, based on FWHM variations in SiV centers in nanodiamonds [22], we propose non-uniform strain to be present in the local environment of the NCD at different locations on the sample.

For comparison, the CVD diamond process in the presence of SnO_2 was also carried out on MCD substrates. Prior to the CVD diamond growth, MCD sub-

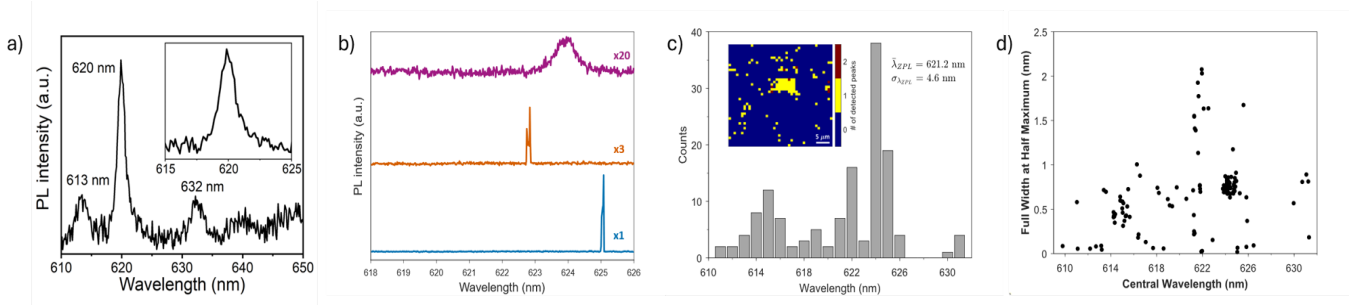


Figure 2. Representative PL spectra of NCD on Si substrate recorded at a) 300 K, b) 7.5 K. The spectra in (b) are vertically offest for clarity and multiplied by the indicated factors, c) central wavelength histogram of detected spectral peaks at 7.5 K with the corresponding PL map (inset), d) distribution of the central wavelength and the FWHM of detected peaks from the same PL map.

strate characterization was carried out using electron backscatter diffraction (EBSD) and room temperature PL techniques. Figure 3 shows the typical EBSD results

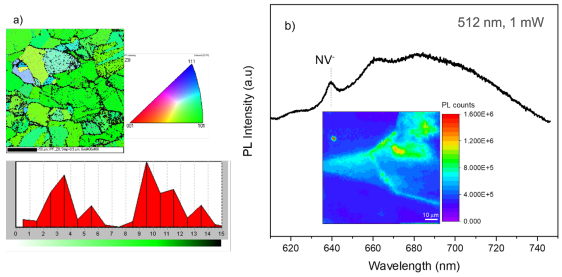


Figure 3. a) EBSD mapping and b) the corresponding room temperature PL characterization results of the MCD substrate. The MCD substrate has a predominant (110) grain orientation with an off-angle of less than 15° with the negatively charged NV center as the prominent optically active defect.

– the MCD substrate has a predominant (110) grain orientation with an off-angle of less than 15°. The PL measurements (Fig. 3 (b)) confirm NV centers in the MCD substrate, indicated by the ZPL at about 638 nm along with its phonon sideband, are the prominent optically active defects along with luminescent grain boundaries detected as the bright regions in the PL mapping.

Diamond growth was carried out with the same process gas ratio as the NCD sample, simultaneously exposing the MCD substrate and pellet of SnO_2 to the diamond growth conditions for a duration of 3 h. We further alleviated Sn coverage of the substrate at an elevation of 3 mm and lateral distance of 5 mm from the dopant source and duly note that placing the MCD substrate further into the plasma results in a higher substrate temperature. To maintain the substrate temperature at 750 °C and 850 °C, MW power of 3000 W and 3500 W with working pressure set to 45 Torr were used, respectively and are henceforth named S750 and S850 in this manuscript. Sn deposists can be seen on the sample surface and after CVD diamond process the samples were wet-chemically etched using the earlier mentioned procedure, followed by inspection with an optical microscope (model: Zeiss Axiovert 40 MAT) to identify areas of the overgrown diamond and subsequent room temperature PL characterization. We also note trapped Sn deposits within the overgrown diamond layer; thus, the overgrown diamond film thickness is not accurately measurable. We estimate a film thickness of about 5 ± 2 µm from the depth scans carried out on the sample using the confocal PL measurement setup.

Figure 4(a) shows a typical room temperature PL spectrum of the S850 sample. The most intense peak at ≈ 738 nm corresponds to the well-known ZPL of SiV centers in diamond [23]. Si is an unintentional dopant in this process, and its origins are speculated to be residual Si or chamber quartz parts of the CVD deposition system [20]. In addition to SiV, spectral features of the NV center at 639 nm and peaks centered at about 620 nm and 631 nm are also identifiable in the PL spectrum. In our experiments, the spectral feature around 620 nm is observed only in the diamond samples deposited in the presence of the Sn dopant source and comparable to the ZPL of SnV in CVD diamond reported in the literature [17].

From the above results, we conclude that our approach incorporates Sn in the lattice and successfully creates SnV centers in diamond using the MW PE CVD technique with SnO_2 as the solid dopant source. We also note that the 631 nm PL peak is reported as the quasi-local vibrations of the impurity atom in the diamond lattice reported by Tchernij et al [24]. We occasionally observe the 631 nm PL peak without an accompanying SnV ZPL, thereby suggesting different origins of the spectral line that are currently unknown or a Sn-related defect. In the literature, the sideband spectrum of the negatively charged SnV center is characterized by the presence of six spectral lines observed at about 634 nm, 644.5 nm, 656 nm, 660 nm, 669.5 nm and 681 nm [25]. Emission lines at 647 nm,and 663 nm, are also reported for the SnV center in diamond fabricated using ion implantation-annealing technique [26]. In the room temperature PL sideband spectra of the S850 sample, we do not identify

the peaks mentioned above, including the most dominant sideband peak at 660 nm / 663 nm. Alternatively, the intense sideband of the negatively charged NV center within this spectral range probably hinders the identification of the SnV sideband PL peak in the sample. Studies of the PL sideband spectra are hence of interest and will be focused in future investigation.

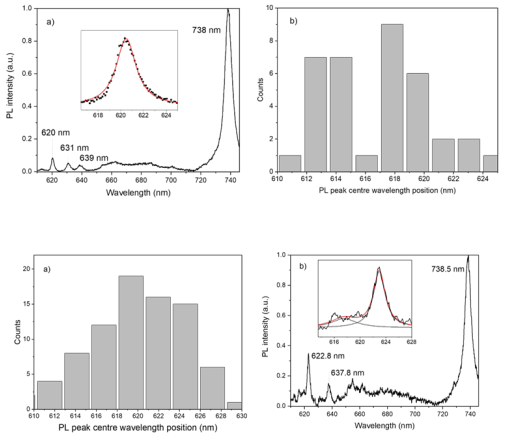


Figure 4. a) An exemplary room temperature PL spectrum of S850 the corresponding histogram of observed PL peaks of sample S850 (a), (b), and S750 (c), (d).

Similar to SiV and GeV centers, the ZPL position of the SnV center in diamond changes with the isotopic constitution of the element and is strain-dependent [20, 22]. Narita et al. reported a difference in ZPL due to Sn isotopes being relatively small [27], thus the ZPL shift observed in our sample is likely to be associated with the strained environment of the SnV center resulting from diamond growth conditions. In addition, the trapped Sn deposits within the overgrown CVD diamond layer may also contribute to the strained environment of the SnV center in our sample. Hence, variations in the SnV ZPL center wavelength position can be expected. Figure 4(b) shows the distribution of PL peaks in sample S850, with the most frequent occurrence of the PL peaks between 612 nm and 620 nm. Sedov et al. also reported observation for strain-associated ZPL shifts of the SnV center in CVD diamond microcrystals, suggesting a spectral shift up to 10 nm [17]. Presently, only few studies report ZPL shift of SnV centers in diamond [28] and the optical properties of SnV centers in diamond under axial stress are currently unavailable in the literature. It is thus challenging to discern the stress response of the SnV ZPL and the range of SnV ZPL from the histogram in Figure 4(b). Furthermore, we note that the SnV center creation in sample S850 is sparse with a high spatial non-uniformity.

The fabrication of SnV in diamond is particularly challenging as Group IV elements have a larger atomic size and their incorporation nto the diamond lattice can be limited. Secondly, the presence of lighter elements such as oxygen, nitrogen, and hydrogen inhibit Sn incorporation in diamond as reported for the HPHT SnV process shows [12]. The hydrogen-rich environment of the CVD growth plasma may be considered unfavorable for SnV generation in diamond as the weaker bond energy of Sn-C relative to the C-C and C-H bonds inhibit Sn incorporation in diamond. Nonetheless, our experimental results and the previous studies by Westerhausen et al. and Sedov et al. show that SnV centers in diamond can be fabricated using the CVD technique [16, 17]. Further, in the following section, we report an improved SnV creation in diamond using a lower substrate temperature.

Figures 4(c) and 4(d) show the histogram of the observed PL peaks in the S750 sample occurring between 610 nm and 630 nm and a representative PL spectrum recorded in the sample S750, respectively. Similar to the S850 sample, the ZPL of the SiV defect remains the most intense also in the S750 sample. Interestingly, the room temperature PL spectra of S750 have an increased ZPL intensity of SnV relative to the S850 sample. The SnV ZPL intensity differences are evident when comparing the PL spectra of S850 (Fig. 4(a) and S750 (Fig. 4(d)). Both the spectra are normalized to the ZPL of the SiV defect in their respective samples. This observation supports that there is an increased SnV generation in CVD diamond at a lower substrate temperature of 750 °C. We also observe an increase in the NV center ZPL intensity and its associated phonon sideband in the sample S750. In our experiments, the base pressure of the MW PE CVD system used is around 5e-3 mbar. Thus, nitrogen can be expected in the CVD growth plasma. Similar results of temperature-dependent N incorporation and enhancement of NV center formation at 700 °C – 760 °C CVD diamond growth temperature are reported in the literature[29, 30].

There are also deviations from this observation of prominent SnV ZPL in the S750 sample. SnV ZPL with low intensity is occasionally seen, as shown in Fig.5(a). It

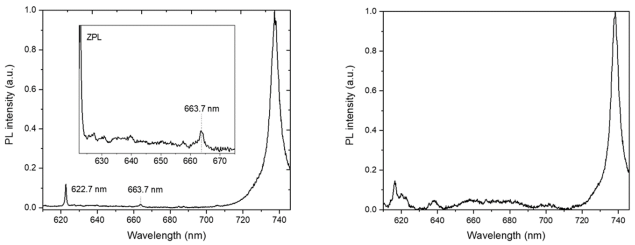


Figure 5. Examples of room temperature PL spectra of sample S750.

should be highlighted that in the absence of the NV center sideband, the 663 nm PL peak can be identified. This observation of the most dominant sideband spectral line of the SnV center supports our previous conclusion that the NV center sideband peaks hinder the identification of the SnV-associated PL peaks in our samples. Another

	Supercell	4×4×4	5×5×5	Infinite-limit	ZPL shift PBE	ZPL shift HSE06
SnV^0	ZPL_{GS}	553.39	562.16	571.36	1.32	0.64
SnV^{-1}	ZPL_{GS}	491.11	494.73	498.53	1.00	0.89
SnV^0	$ZPL_{\Delta E}$	599.62	603.04	606.63	1.15	1.36
SnV^{-1}	$ZPL_{\Delta E}$	590.82	594.08	597.50	1.40	1.37

Table I. Calculated ZPL position at the HSE06 level of theory. All values are given in nm. The infinite dilute limit is calculated as linear extrapolation from the given supercells. The size of the ZPL shift is given in nm/GPa, as obtained for the 4×4×4 and 5×5×5 supercell, for both PBE and HSE06 functionals. In case of compressive/tensile strain the ZPL is blue/red shifted.

relevant observation from the room temperature PL analysis is an improved spatial uniformity of SnV creation in sample S750. The SnV ZPL peaks around 620 nm are observed more often in the S750 than in the S850 sample for a comparable PL scan area (see Fig. 4(a)). Similar to the sample S850, PL peak shifts are observed in the sample S750. From these observations, we conclude that the S750 sample was grown under CVD conditions that promote SnV creation in diamond. We also note that due to the lower substrate temperature, features such as dislocations can be observed on the S750 sample surface, suggesting non-ideal diamond growth conditions. On the contrary, the S850 sample deposited at a higher growth temperature is devoid of such features. These results indicate the limitations of the process: a lower substrate temperature promotes SnV creation in diamond with improved spatial uniformity, while SnV centers in diamond are sparsely fabricated at a high substrate temperature. We also note that these crystallographic defects in the S750 sample may lead to additional and complex PL peak structures, as shown in Figure 5(b). As mentioned earlier, there are limited studies on the strain dependence of the SnV center in diamond. Such PL features will be interesting for future studies.

To gain theoretical insights, a set of density functional theory (DFT) calculations was performed to investigate the effect of hydrostatic strain on the SnV^0 and SnV^- defect in diamond. The calculations were performed on supercells with 512 and 1000 atoms, using a Gamma-only k-point set. The structure was optimized using the PBE functional (as it is more cost-effective than HSE) and high accuracy electronic structure calculations were performed using the HSE functional. For the latter a two-step approach was used to reduce the computational cost. More details on the computational methods can be found in the Supporting Information section.

We calculated the ZPL position and shift due to hydrostatic strain for a defect concentration of 0.195% (4×4×4 supercell) and 0.1% (5×5×5 supercell). The neutral and negative charge state of SnV are considered, though it should be stressed that both SnV^0 and SnV^- centres draw a significant amount of electrons from their environment, giving rise to a negatively charged defect (spatial charge), as can be seen from the calculated Hirshfeld-I charges [31, 32]. This spatial charge accumulation also contributes to the size the SnV center, resulting in a size equivalent to 3.8 – 5 carbon atoms. Similar to the GeV center, there is a significant supercell size dependence for both the SnV^0 and SnV^- centre [33]. Assuming a linear trend, as was observed for the GeV case, the infinite dilute limit was calculated to better approximation for the experimental ppm level concentration.

As seen in Table I, the calculated ZPL energy is slightly overestimated using the HSE06 functional resulting in a lower wavelength than experimentally observed, similar as was observed for the GeV system. Our calculated value of 590.92 nm (2.099 eV) for the $ZPL_{\Delta E}$ energy of SnV^- using the 4×4×4 supercell is in very good agreement with the value of 587.6 nm (2.11 eV) presented by Gali and Thiering for the same supercell and functional, though they applied a C_{2h} symmetry to the defect to account for Jahn Teller distortion. Furthermore, their calculations also show that the incorporation of spin-orbit coupling lowers this energy by about 20 meV to 2.09 eV (593.23 nm) .

Despite the limitations with regard to absolute ZPL positions, DFT can provide valuable insights with regard to relative positioning and shifts. Fist of all, we note that the $ZPL_{\Delta E}$ values are closer to the experimental observation, which can be understood from the fact that DFT is a ground state theory, and as such, position of empty states are poorly described. Using the energy difference of the ground state with the adiabatic excitation energy corresponds to a constrained 'ground state' calculations, which is better described by DFT. For both approaches, it is shown that the SnV^0 is located at a higher wavelength than the SnV^-, with the difference being a mere 9 nm for the more accurate $ZPL_{\Delta E}$ approach. This may make them hard to distinguish solely based on the ZPL position. The ZPL shift was calculated using the PBE and HSE06 functional, for both the 4×4×4 and 5×5×5 supercell, with the external pressure obtained from fitting the energy-volume data to the Rose-Vinet equation of state.

For the SnV^0, the ZPL-shift is about three times larger than was previously reported for the GeV^0. Similar as for the GeV system, it is noted that the ZPL is red-shifted in case of tensile strain, while a compressive hydrostatic strain results in a blue-shift of the ZPL. Considering the more accurate $ZPL_{\Delta E}$ approach, the PBE and HSE06

results are almost the same. More importantly, also the shift of the SnV^0 and $SnV^-$are roughly (PBE) to almost exactly (HSE06) the same, with a shift of $1.37\,\mathrm{nm\,GPa^{-1}}$ for hydrostatic conditions.

In a polycrystalline diamond sample, residual stress due to local defects and grain boundaries are expected, though the induced stress may be limited to only a few GPa. This would give rise to red and blue shifted ZPL of a few nm. Note however that in case of the GeV^0 it was shown that linear strain gives rise to much larger shifts which could explain the larger observed shifts in this study.

To conclude, in this study we report the fabrication of SnV centers in NCD and free-standing (110)-oriented MCD discs using the MW PE CVD technique with SnO_2 pellets as the solid dopant source. Room temperature PL measurements confirm the presence of SnV centers in diamond with spatial noun-uniformity. In addition to the ZPL at 620 nm, PL peak shifts are observed in both NCD and MCD samples. We attribute these PL peak shifts to non-uniformity in strain and masking of the fine structure of the spectral line at cryogenic temperature PL spectra to morphological imperfections of the diamond lattice. Using SnO_2 as the dopant source leads to Sn deposits on the sample surface leading to partial substrate coverage and limiting diamond growth. Using a modified substrate holder, we have partially alleviated the coverage of Sn on the MCD substrate during diamond growth. Our results show a temperature-dependent creation of the SnV centres in CVD diamond layers. CVD diamond growth temperature of 850° leads to sparse SnV creation in diamond, while a lower substrate temperature of 750° leads to an improved spatial uniformity with a simultaneous enhancement of SnV ZPL intensity. In both samples, PL peak shifts are observed, and we attribute them to the strained environment of the SnV center. Theoretical studies on the SnV center under hydrostatic conditions show similar trends to the previously reported studies on the GeV center in diamond, a shift of $1.37\,\mathrm{nm\,GPa^{-1}}$ for hydrostatic conditions can be expected. These findings provide important insights for optimizing the fabrication of SnV centers in diamond using the microwave plasma-enhanced chemical vapor deposition technique, with potential applications in quantum technologies.

NOTES

The authors declare no competing financial interests.

ACKNOWLEDGEMENT

The authors thank the funding from the Special Research Fund (BOF) via Methusalem NANO network, and interuniversity BOF (BOF23IU12).

REFERENCES

[1] K. Nemoto, M. Trupke, S. J. Devitt, A. M. Stephens, B. Scharfenberger, K. Buczak, T. Nöbauer, M. S. Everitt, J. Schmiedmayer, W. J. Munro, Photonic architecture for scalable quantum information processing in diamond, Physical Review X 4 (2014) 031022. doi:10.1103/PhysRevX.4.031022.

[2] M. Ruf, N. H. Wan, H. Choi, D. Englund, R. Hanson, Quantum networks based on color centers in diamond, Journal of Applied Physics 130 (8 2021). doi:10.1063/5.0056534.

[3] D. A. Golter, G. Clark, T. E. Dandachi, S. Krastanov, A. J. Leenheer, N. H. Wan, H. Raniwala, M. Zimmermann, M. Dong, K. C. Chen, L. Li, M. Eichenfield, G. Gilbert, D. Englund, Selective and scalable control of spin quantum memories in a photonic circuit, Nano Letters 23 (2023) 7852–7858. doi:10.1021/acs.nanolett.3c01511.

[4] C. Osterkamp, M. Mangold, J. Lang, P. Balasubramanian, T. Teraji, B. Naydenov, F. Jelezko, Engineering preferentially-aligned nitrogen-vacancy centre ensembles in cvd grown diamond, Scientific Reports 9 (2019) 5786. doi:10.1038/s41598-019-42314-7.

[5] K. Liu, S. Zhang, V. Ralchenko, P. Qiao, J. Zhao, G. Shu, L. Yang, J. Han, B. Dai, J. Zhu, Tailoring of typical color centers in diamond for photonics, Advanced Materials 33 (2 2021). doi:10.1002/adma.202000891.

[6] L. V. H. Rodgers, L. B. Hughes, M. Xie, P. C. Maurer, S. Kolkowitz, A. C. B. Jayich, N. P. de Leon, Materials challenges for quantum technologies based on color centers in diamond, MRS Bulletin 46 (2021) 623–633. doi:10.1557/s43577-021-00137-w.

[7] T. Iwasaki, Chapter eight - color centers based on heavy group-iv elements, in: C. E. Nebel, I. Aharonovich, N. Mizuochi, M. Hatano (Eds.), Diamond for Quantum Applications Part 1, Semiconductors and Semimetals, Elsevier, 2020, pp. 237–256. doi:https://doi.org/10.1016/bs.semsem.2020.03.007.

[8] D. Chen, N. Zheludev, W. Gao, Building blocks for quantum network based on group-iv split-vacancy centers in diamond, Advanced Quantum Technologies 3 (2 2020). doi:10.1002/qute.201900069.

[9] C. Bradac, W. Gao, J. Forneris, M. E. Trusheim, I. Aharonovich, Quantum nanophotonics with group iv defects in diamond, Nature Communications 10 (2019) 5625. doi:10.1038/s41467-019-13332-w.

[10] M. Ruf, N. H. Wan, H. Choi, D. Englund, R. Hanson, Quantum networks based on color centers in diamond, Journal of Applied Physics 130 (7) (2021).

[11] T. Iwasaki, Y. Miyamoto, T. Taniguchi, P. Siyushev, M. H. Metsch, F. Jelezko, M. Hatano, Tin-vacancy quantum emitters in diamond, Physical Review Letters 119 (2017) 253601. doi:10.1103/PhysRevLett.119.253601.

[12] E. A. Ekimov, S. G. Lyapin, M. V. Kondrin, Tin-vacancy color centers in micro- and polycrystalline diamonds synthesized at high pressures, Diamond and Related Materials 87 (2018) 223–227. doi:10.1016/j.diamond.2018.06.014.

[13] Y. N. Palyanov, I. N. Kupriyanov, Y. M. Borzdov, High-pressure synthesis and characterization of sn-doped single crystal diamond, Carbon 143 (2019) 769–775. doi:10.1016/j.carbon.2018.11.084.

[14] A. E. Rugar, H. Lu, C. Dory, S. Sun, P. J. McQuade, Z.-X. Shen, N. A. Melosh, J. Vučković, Generation of tin-vacancy centers in diamond via shallow ion implantation and subsequent diamond overgrowth, Nano Letters 20 (2020) 1614–1619. doi:10.1021/acs.nanolett.9b04495.

[15] M. Fujiwara, M. Ohori, F. T. K. So, Y. Makino, N. Morioka, I. Ohki, R. Igarashi, M. Nishikawa, N. Mizuochi, Single tin-vacancy center in nanoscale diamond, Discover Nano 20 (1) (2025) 81. doi:10.1186/s11671-025-04256-0.

[16] M. T. Westerhausen, A. T. Trycz, C. Stewart, M. Nonahal, B. Regan, M. Kianinia, I. Aharonovich, Controlled doping of gev and snv color centers in diamond using chemical vapor deposition, ACS Applied Materials & Interfaces (2020) acsami.0c07242doi:10.1021/acsami.0c07242.

[17] V. Sedov, A. Martyanov, A. Neliubov, I. Tiazhelov, S. Savin, I. Eremchev, M. Eremchev, M. Pavlenko, S. Mandal, V. Ralchenko, A. Naumov, Narrowband photoluminescence of tin-vacancy colour centres in sn-doped chemical vapour deposition diamond microcrystals, Philosophical Transactions of the Royal Society A: Mathematical, Physical and Engineering Sciences 382 (1 2024). doi:10.1098/rsta.2023.0167.

[18] R. Mary Joy, P. Pobedinskas, N. Baule, S. Bai, D. Jannis, N. Gauquelin, M.-A. Pinault-Thaury, F. Jomard, K. J. Sankaran, R. Rouzbahani, F. Lloret, D. Desta, J. D'Haen, J. Verbeeck, M. F. Becker, K. Haenen, The effect of microstructure and film composition on the mechanical properties of linear antenna cvd diamond thin films, Acta Materialia 264 (2024) 119548. doi:https://doi.org/10.1016/j.actamat.2023.119548.

[19] T.-T.-N. Nguyen, M. Sasaki, S.-N. Hsiao, T. Tsutsumi, K. Ishikawa, M. Hori, Low-temperature reduction of sno2 by floating wire-assisted medium-pressure h2/ar plasma, Plasma Processes and Polymers 19 (6), cited by: 12 (2022). doi:10.1002/ppap.202100209.

[20] R. M. Joy, P. Pobedinskas, E. Bourgeois, T. Chakraborty, J. Goerlitz, D. Herrmann, C. Noel, J. Heupel, D. Jannis, N. Gauquelin, J. D'Haen, J. Verbeeck, C. Popov, L. Houssiau, C. Becher, M. Nesládek, K. Haenen, Photoluminescence of germanium-vacancy centers in nanocrystalline diamond films: Implications for quantum sensing applications, ACS Applied Nano Materials 7 (2024) 3873–3884. doi:10.1021/acsanm.3c05491.

[21] R. Nelz, J. Görlitz, D. Herrmann, A. Slablab, M. Challier, M. Radtke, M. Fischer, S. Gsell, M. Schreck, C. Becher, E. Neu, Toward wafer-scale diamond nano- and quantum technologies, APL Materials 7 (1) (2019) 011108. doi:10.1063/1.5067267.

[22] S. Lindner, A. Bommer, A. Muzha, A. Krueger, L. Gines, S. Mandal, O. Williams, E. Londero, A. Gali, C. Becher, Strongly inhomogeneous distribution of spectral properties of silicon-vacancy color centers in nanodiamonds, New Journal of Physics 20 (2018) 115002. doi:10.1088/1367-2630/aae93f.

[23] C. Chen, Y. Mei, J. Cui, X. Li, M. Jiang, S. Lu, X. Hu, Man-made synthesis of ultrafine photoluminescent nanodiamonds containing less than three silicon-vacancy colour centres, Carbon 139 (2018) 982–988. doi:https://doi.org/10.1016/j.carbon.2018.08.013.

[24] S. D. Tchernij, T. Herzig, J. Forneris, J. Küpper, S. Pezzagna, P. Traina, E. Moreva, I. P. Degiovanni, G. Brida, N. Skukan, M. Genovese, M. Jakšić, J. Meijer, P. Olivero, Single-photon-emitting optical centers in diamond fabricated upon sn implantation, ACS Photonics 4 (2017) 2580–2586. doi:10.1021/acsphotonics.7b00904.

[25] J. Görlitz, D. Herrmann, G. Thiering, P. Fuchs, M. Gandil, T. Iwasaki, T. Taniguchi, M. Kieschnick, J. Meijer, M. Hatano, A. Gali, C. Becher, Spectroscopic investigations of negatively charged tin-vacancy centres in diamond, New Journal of Physics 22 (2020) 013048. doi:10.1088/1367-2630/ab6631.

[26] E. Corte, S. Sachero, S. D. Tchernij, T. Lühmann, S. Pezzagna, P. Traina, I. P. Degiovanni, E. Moreva, P. Olivero, J. Meijer, M. Genovese, J. Forneris, Spectral emission dependence of tin-vacancy centers in diamond from thermal processing and chemical functionalization, Advanced Photonics Research 3 (1 2022). doi:10.1002/adpr.202100148.

[27] Y. Narita, P. Wang, K. Ikeda, K. Oba, Y. Miyamoto, T. Taniguchi, S. Onoda, M. Hatano, T. Iwasaki, Multiple tin-vacancy centers in diamond with nearly identical photon frequency and linewidth, Phys. Rev. Appl. 19 (2023) 024061. doi:10.1103/PhysRevApplied.19.024061.

[28] B. Vindolet, M.-P. Adam, L. Toraille, M. Chipaux, A. Hilberer, G. Dupuy, L. Razinkovas, A. Alkauskas, G. Thiering, A. Gali, M. D. Feudis, M. W. N. Ngambou, J. Achard, A. Tallaire, M. Schmidt, C. Becher, J.-F. Roch, Optical properties of siv and gev color centers in nanodiamonds under hydrostatic pressures up to 180 gpa, Physical Review B 106 (2022) 214109. doi:10.1103/PhysRevB.106.214109.

[29] A. Tallaire, M. Lesik, V. Jacques, S. Pezzagna, V. Mille, O. Brinza, J. Meijer, B. Abel, J. Roch, A. Gicquel, J. Achard, Temperature dependent creation of nitrogen-vacancy centers in single crystal cvd diamond layers, Diamond and Related Materials 51 (2015) 55–60. doi:10.1016/j.diamond.2014.11.010.

[30] J. Prooth, M. Petrov, A. Shmakova, M. Gulka, P. Cigler, J. D'Haen, H. Boyen, M. Nesladek, Long spin relaxation times in cvd-grown nanodiamonds, Advanced Quantum Technologies 6 (12 2023). doi:10.1002/qute.202300004.

[31] D. E. P. Vanpoucke, P. Bultinck, I. V. Driessche, Extending hirshfeld-i to bulk and periodic materials, Journal of Computational Chemistry 34 (2013) 405–417. doi:10.1002/jcc.23088.

[32] D. E. P. Vanpoucke, I. V. Driessche, P. Bultinck, Reply to 'comment on "extending hirshfeld-i to bulk and periodic materials"', Journal of Computational Chemistry 34 (2013) 422–427. doi:10.1002/jcc.23193.

[33] T. G. van Wijk, E. A. Melan, R. Mary Joy, E. Y. Guillaume, P. Pobedinskas, K. Haenen, D. E. Vanpoucke, The impact of strain on the GeV-color center in diamond, Carbon 234 (2025) 119928. doi:10.1016/j.carbon.2024.119928.

[34] G. Kresse, D. Joubert, From ultrasoft pseudopotentials to the projector augmented-wave method, Physical Re-

view B 59 (1999) 1758–1775. doi:10.1103/PhysRevB.59.1758.

[35] J. P. Perdew, K. Burke, M. Ernzerhof, Generalized gradient approximation made simple, Physical Review Letters 77 (1996) 3865–3868. doi:10.1103/PhysRevLett.77.3865.

[36] J. Heyd, G. E. Scuseria, M. Ernzerhof, Hybrid functionals based on a screened coulomb potential, The Journal of Chemical Physics 118 (2003) 8207–8215. doi:10.1063/1.1564060.

[37] J. Heyd, G. E. Scuseria, M. Ernzerhof, Erratum: "hybrid functionals based on a screened coulomb potential" [j. chem. phys. 118, 8207 (2003)], The Journal of Chemical Physics 124 (6 2006). doi:10.1063/1.2204597.

[38] G. Thiering, A. Gali, Ab initio magneto-optical spectrum of group-iv vacancy color centers in diamond, Physical Review X 8 (2018) 021063. doi:10.1103/PhysRevX.8.021063.

[39] P. Vinet, J. R. Smith, J. Ferrante, J. H. Rose, Temperature effects on the universal equation of state of solids, Physical Review B 35 (1987) 1945–1953. doi:10.1103/PhysRevB.35.1945.

[40] A. Gali, J. R. Maze, Ab initio study of the split silicon-vacancy defect in diamond: Electronic structure and related properties, Physical Review B 88 (2013) 235205. doi:10.1103/PhysRevB.88.235205.

SUPPORTING INFORMATION

Film characterization details

Raman measurements were carried out using a 532 nm laser with a Renishaw inVia confocal Raman microscope. Electron backscatter diffraction (EBSD) was carried out using a system from HHL Technology, integrated into a Quanta 200 FEG scanning electron microscope (SEM) manufactured by FEI. The typical penetration depth of the electron beam in EBSD is tens of nanometers and provides surface crystallographic orientation data of individual grains.

Room temperature photoluminescence (PL) measurements are carried out using Quantum Gem laser with 512 nm wavelength and 1 mW power, focused via an objective with a numerical aperture of 0.95. For the SnV ZPL detection, a band-pass filter (ThorLabs FB620-10, center wavelength = (620 ± 2) nm, Full Width Half Maximum = (10 ± 2) nm) is used in the PL detection path for mapping. For measurements at cryogenic temperatures, a continuous-flow helium-based optical cryostat (attoDRY800) was used and a base temperature of 7.5 K in the sample holder was reached. The sample holder is equipped with three linear piezoelectric positioners with sub-micrometer precision that were used to perform spatial mappings of the samples PL. A continuous wave green laser (CNI MGL-FN-532) operating at 532 nm was used as an excitation source with a power of 10 mW. The measurements were performed in a confocal configuration using a 100× and 0.70 NA microscope objective for both the focusing of the excitation source and the collection of the PL. The PL spectra were measured using an Andor Shamrock 750 spectrograph coupled to an Andor Newton EMCCD. After calibrating the spectrometer gratings to the emission lines of a Neon lamp, the wavelength uncertainty of the spectrometer was found to be below 0.5 nm across the wavelength range of interest.

Computational details

The SnV color center was modeled using conventional 4×4×4 and 5×5×5 supercells of 512 and 1000 atoms, respectively. In these supercells, two neighboring carbon atoms were replaced by a single Sn atom. After structure optimization, the latter was moved to the center of the former C-C bond, resulting in the well-known split-vacancy configuration. The bond lengths and defect properties for the neutral and negatively charged defects are listed in Table II.

First-principles quantum mechanical calculations were performed within the framework of DFT using the projector augmented waves method as implemented in VASP [34]. For C and Sn the $2s^2 2p^2$ and $4d^{10} 5s^2 5p^2$ electrons were considered as valence electrons. For structure optimization, a generalized gradient approximation was used to describe exchange-correlation behavior, specifically the PBE functional [35]. More accurate electronic structure calculations were performed using the HSE06 hybrid functional [36, 37] , using the PBE optimized atomic geometries. Due to the large size of the systems, the reciprocal space was sampled using the Γ-point only, in line with the current state-of-the-art [33, 38]. The effect of hydrostatic pressure was simulated for (isotropic) compressive and tensile strain, by the respective increase or increase of the lattice parameters by ±1, ±2%. These systems were then relaxed under the constraint of a fixed volume and cubic cell shape. Combined with the equilibrium point, the resulting five values allow for a fit to the Rose-Vinet equation of state, [39] which provides access to a pressure volume relation, which can be used to investigate the pressure dependence of the ZPL position [33]. The volume range investigated in this work, corresponds to a pressure range of 17–17.4 GPa. It is worthy to note that the pressure range was almost exactly the same for PBE and HSE06 calculations, with variations of 0.01 GPa or less. For the PBE calculations, the pressure ranges for the different charge states and concentrations ran from about -7.7 GPa to +9.6 GPa, while for the HSE06 case the range was between about -0.4 and -17.8 GPa.

The shift of the ranges is a consequence of the fact that the PBE optimized volumes and structures are also used for the HSE06 calculations, to avoid the excessive computational cost which would be involved in the structure optimization using the latter functional. Note that this will not affect the results regarding the ZPL shift, as this is linear in these low pressure ranges. The SnV charge state is controlled by the manual setting of the number of electrons in the system, and the occupation of the Kohn-Sham orbitals[40]. However, it is also interesting to investigate the local charge accumulation and polarization at the defect site. Using the iterative Hirshfeld atoms-in-molecules partitioning scheme, the atomic charge of each atom was calculated, and the defect charge was defined as the cumulative charge of the Sn atom and its six nearest neighbor carbon atoms[31, 32].

To model the ZPL position, two approaches were used, firstly, the ZPL was calculated as the energy difference between the Kohn–Sham valence band maximum (VBM) and the empty e_g state (ZPL_{GS}). The choice of using the VBM is based on our previous observation for the GeV center, that the e_u states shift toward the VBM for larger supercells, and are expected to (almost) coincide with the VBM at experimental ppm defect concentrations [33]. Secondly, the ZPL position was approximated as the difference in total energy between the system in the ground state system ($ZPL_{\Delta E}$), and the system with a single electron removed from the VBM and placed in an empty e_g state, upon which the geometry of the excited system was relaxed (i.e. adiabatic excitation energy). At the PBE level, this gives rise to a relaxation energy in the order of 30–40 meV. Here it is also interesting to note that upon relaxation, the e_u states move upward to the VBM level for SnV^-, leading to an effectively empty e_u state.

Cell	Charge state	Sn–C_{Sn} bond length	SnV bond length	Q_{Sn}	Q_{CSn}	Q_{SnV}
4×4×4	0	2.1034	22.737	2.1865	–0.6908	–1.9583
4×4×4	–1	2.1028	29.598	2.2413	–0.7963	–2.5365
5×5×5	0	2.1024	22.779	2.1885	–0.6893	–1.9473
5×5×5	–1	2.1010	29.586	2.2479	–0.7958	–2.5269

Table II. Structural parameters after structure optimization at the PBE level with Sn–C bond length with the six nearest neighbor C atoms (C_{Sn}), the volume of the SnV defect, and the atomic charge of the Sn atom, each of the six C_{Sn} atoms, and the combined charge of the SnV defect using the Hirshfeld-I AIM partitioning scheme [31, 32]